2021 IEEE 22nd Workshop on Control and Modelling of Power Electronics (COMPEL) | 978-1-6654-3635-9/21/$31.00 ©2021 IEEE | DOI: 10.1109/COMPEL52922.2021.9645976

Augmented Piezoelectric Resonators for Power Conversion

Joseph E. Bonavia, Jessica D. Boles, Jeffrey H. Lang, and David J. Perreault
Massachusetts Institute of Technology
Cambridge, MA, USA
Emails: jbonavia@mit.edu, jboles@mit.edu, lang@mit.edu, and djperrea@mit.edu

***Abstract*—With high efficiency and power density at small scales, piezoelectric resonators (PRs) are promising alternatives to magnetic components for miniaturized power conversion. PRs have been demonstrated to be capable of high efficiency in dc-dc converters with favorable scalability to small sizes. In this work, we analytically show that augmenting PRs with mass layers for additional inertial energy storage can further reduce component size while improving efficiency. We model the effects of mass augmentation on the behavior of a PR as well as on its efficiency and power density characteristics. We further provide design guidelines for mass-augmented PRs, which we validate through simulation in COMSOL. It is estimated that for an example case, mass augmentation is capable of decreasing a PR's minimum loss ratio by 44% and increasing its maximum volumetric power density by 130%.**

***Index Terms*—piezoelectric resonator, dc-dc converter, high power density**

I. Introduction

As power electronics are designed to be smaller and lighter, magnetic components become the primary bottlenecks for power density and performance improvement [1], [2]. This motivates investigation into alternative passive component technologies for use in miniaturized power conversion. Piezoelectric components, which store energy in the mechanical compliance and inertia of a piezoelectric material, are one such prospect. Unlike magnetics, piezoelectrics offer very high power density and efficiency capabilities at small scales [3], [4]. Moreover, piezoelectrics offer additional advantages to power conversion including planar form factors, batch fabrication, isolation (with multi-port components), and the potential for a high degree of integration.

Magnetic-less power converters based on piezoelectric resonators (PRs) have been demonstrated to offer high efficiency over wide operating ranges [5]–[8]. Such high-efficiency converter implementations are enumerated in [6] for PRs and in [9] for piezoelectric transformers, resulting in maximum-efficiency topologies like that of Fig. 1. In [4], we establish figures of merit for the evaluation of piezoelectric materials and vibration modes along with PR design criteria for maximum efficiency and power density, and these properties are demonstrated to scale favorably for converter miniaturization.

This material is based upon work supported by a gift from Texas Instruments, the National Science Foundation Graduate Research Fellowship (Grant No. 1122374), and the MIT Undergraduate Research Opportunities Program.

TABLE I
Material State Definitions

u	Mechanical Displacement (m)
T	Mechanical Stress (N/m^2)
S	Mechanical Strain
E	Electric Field Strength (N/m)
D	Electric Flux Density (C/m^2)

TABLE II
Material Property Definitions

Q_M	Mechanical Quality Factor
k_t	Thickness Mode Electromechanical Coupling Factor
ρ	Mass Density (kg/m^3)
ε	Dielectric Constant (F/m)
c	Elastic Modulus (N/m^2)
e	Piezoelectric Strain Modulus (C/m^2)
T_{Max}	Maximum Mechanical Stress (N/m^2)
E_{Max}	Maximum Electric Field Strength (N/m)
H_{Max}	Maximum Loss Density (W/m^2)

Further, design and fabrication of lithium niobate PRs for power conversion is explored in [7].

Although PRs in their typical, non-augmented forms (i.e., "bare" PRs) offer favorable scaling properties for miniaturization, we analytically show that further gains in efficiency and power density could be achieved through PR "augmentation". We define PR augmentation as the addition of mass and/or a spring-like material to the dynamic surfaces of a PR to yield a composite electromechanical energy storage component. In this work, we derive the effects of mass augmentation on a PR's electrical circuit model, its maximum achievable efficiency, and its maximum achievable power density. We further provide design guidelines for mass-augmented PRs, which we validate through simulation.

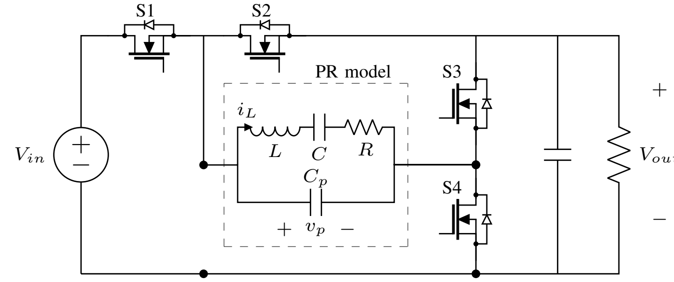

Fig. 1. Example topology for the highest-efficiency switching sequence proposed in [6].

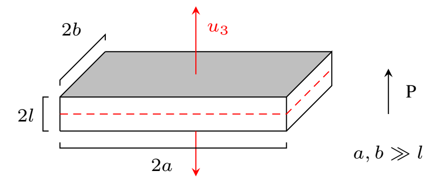

Fig. 2. Thickness extensional vibration mode of a bare PR. Shaded areas denote electrodes. P denotes the polarization direction of the PR, x_3. All surfaces are assumed to be traction-free. Dashed red lines denote the nodal plane ($u_3 = 0$). The origin is taken to be the PR's center.

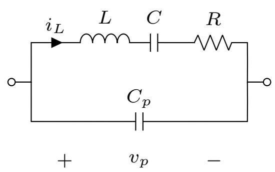

Fig. 3. Butterworth-Van Dyke equivalent circuit model for PRs [10].

TABLE III
BUTTERWORTH-VAN DYKE CIRCUIT MODEL PARAMETERS

C_p	C	L	R
$\epsilon_{33}^S \frac{2ab}{l}$	$\frac{8C_p k_t^2}{\gamma_0^2}$	$\frac{l^2}{2C_p k_t^2 v_a^2}$	$\frac{1}{4Q_M} \frac{l\gamma_0}{C_p k_t^2 v_a}$

where $\gamma_0 = \sqrt{\pi^2 - 8k_t^2}$

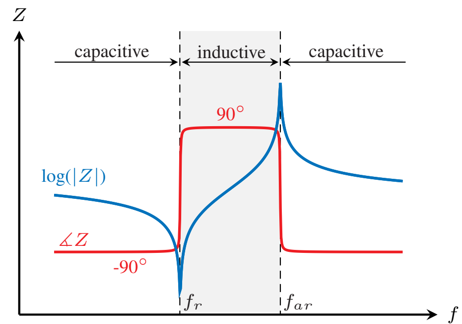

Fig. 4. PR impedance in the proximity of a vibration mode, where f_r is the resonant frequency and f_{ar} is the anti-resonant frequency. The inductive region between the resonant and anti-resonant frequency is of most interest to power conversion.

II. Modeling Augmentation

To evaluate the power conversion capabilities of a mass-augmented PR, it is important to first derive its equivalent electrical circuit model. In this section, we begin by introducing a widely-accepted model for bare PRs and then illustrate how this model changes with mass augmentation.

A. Bare Piezoelectric Resonator Model

A PR's behavior is dictated by its material's constitutive relations and equation of motion, which collectively produce an acoustic wave equation. In this work, excitation of purely the fundamental resonant frequency of a PR's thickness extensional vibration mode is assumed. Therefore, the resulting wave equation can be assumed to have a purely sinusoidal solution for displacement, u_3:

$$u_3(x_3, t) = \Delta \sin(\kappa x_3) e^{j\omega t} \tag{1}$$

where κ (in rad) is the wave number and ω (in $\frac{rad}{s}$) is the wave's radial frequency of vibrations. Power converters excite the PR with a periodic voltage excitation, so ω is set by a converter's switching frequency. It is also helpful to define κ_0 to be the geometry-normalized wave number:

$$\kappa_0 = \kappa * l \tag{2}$$

which describes the portion of the acoustic wave (in radians) that is completed over the PR's half-length l. The acoustic wave's frequency f (in Hz) can be related to the other PR wave parameters using:

$$f = \frac{\omega}{2\pi} = \frac{\kappa v_a}{2\pi} = \frac{\kappa_0 v_a}{2\pi l}, \tag{3}$$

where v_a (in $\frac{m}{s}$) is the acoustic velocity of the piezoelectric material, or $\sqrt{\frac{c_{33}^D}{\rho}}$ as defined in [11].

In order to solve for the forms of the state variables, (1) is inserted into the constitutive equations, and the traction-free boundary condition

$$T_3(x_3 = \pm l) = 0 \tag{4}$$

(which assumes no externally applied forces on the outer surfaces of the PR) is enforced. Integrating the electric field, E and flux density D in space results in the forms of the PR's voltage and current, and from them the form of the PR's electrical impedance (Z). After approximating a tangent term with the first term of its partial fraction expansion (detailed in Appendix A), the impedance is then set directly equal to the impedance of the previously-established Butterworth-Van Dyke (BVD) circuit model shown in Fig. 3 [10]. From this, the values of L, C, C_p, and R in Table III can be retrieved. A more detailed derivation for these parameters can be found in [11] and [4]. Fig. 4 displays a plot of the bare PR's impedance.

B. Mass-Augmented Piezoelectric Resonator Model

To illustrate the effects of PR augmentation, we focus on the mass-augmented PR example shown in Fig. 5. Throughout this work, the subscript m denotes a property of the added mass layer. The values of the dimensions a, b, and l are assumed to be the same in both the bare and mass-augmented case (although the scaling relationships derived in Sections III and IV will be entirely independent of PR geometry).

We model the additional mass layers as rigid (non-deformable) bodies of mass m_m and thickness $\beta * l$ attached to the free ends of the PR ($x_3 = l$ and $x_3 = -l$). This necessitates the boundary condition:

$$T_3(x_3 = \pm l) = -\frac{m_m \ddot{u}}{4ab} = -\rho_m \beta l \frac{\partial^2 u}{\partial t^2} \tag{5}$$

(which comes directly from Newton's Second Law for a rigid body, $F = ma$) in place of (4). An analysis of the validity of this rigid body assumption is included in Appendix B.

The same sinusoidal form (1) is assumed for the displacement, u, in the piezoelectric layer and this new PR system is again solved for the new forms of the other state variables

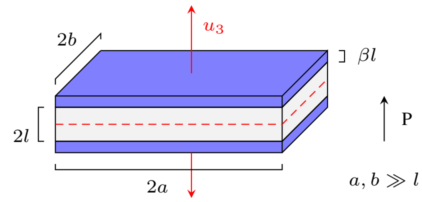

Fig. 5. Thickness vibration mode of a mass-augmented PR of density ρ. A layer of mass of density ρ_m and thickness βl (blue) has been added to both electrodes. The origin is again taken to be the center of the PR.

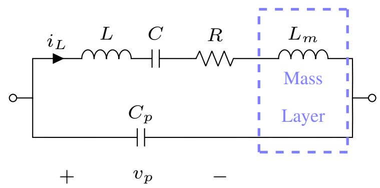

Fig. 6. Equivalent circuit model for a mass-augmented PR, where L_m represents added inductance due to the mass.

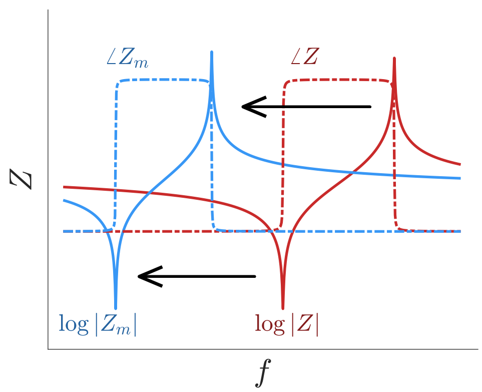

Fig. 7. Example impedance shift due to mass augmentation of a PR.

(T, D, and E), voltage, and current. This results in a different impedance for the mass-augmented PR, Z_m. Tangent terms in Z_m are again approximated with the partial fraction expansion, and Z_m is matched to the equivalent circuit in Fig. 6. In this circuit, the added mass takes the form of an additional inertial inductor:

$$L_m = 2\beta \frac{\rho_m}{\rho} L \tag{6}$$

while all other circuit parameters remain the same. This additional inductor is corroborated in [12], and an expression with a similar form to L_m is included in [13] (both for sensing applications). This "mass inductance" has the effect of shifting the entire impedance plot (and by extension the inductive region) downward in frequency as shown in Fig. 7.

III. Effect of Augmentation on Efficiency

If the added mass can be approximated as a rigid body, it can be assumed that all loss occurs in the piezoelectric material layer of the augmented PR (as in the bare case). However, the added mass does store additional energy through its inertia. For this reason, mass augmentation increases efficiency. In this section, we model the scale of this effect on efficiency.

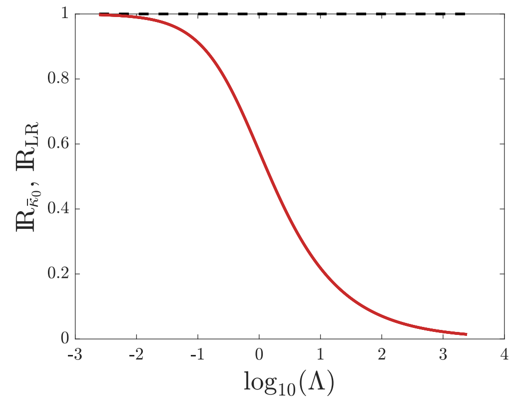

Fig. 8. Geometry-normalized wave number and loss ratio scaling as a function of mass factor, Λ, (defined in (11)) for a mass-augmented PR.

A. Defining Minimum Loss Ratio

In order to quantify efficiency, it is necessary to define a loss ratio:

$$LR = \frac{P_{loss}}{P_{out}} \tag{7}$$

which represents the ratio of the power dissipated (due to mechanical interactions in the PR), P_{loss}, to the power delivered to the load, P_{out}. LR can then be minimized over geometric parameter $G = \frac{4ab}{l^2}$ [4]. Through this minimization, it be shown that maximum-efficiency operation only occurs at a set value for f (and by extension κ_0). We define the value of κ_0 at this maximum efficiency operating point as:

$$\bar{\kappa}_0 = \frac{\pi\gamma_0}{\pi + \gamma_0} \tag{8}$$

where $\gamma_0 = \sqrt{\pi^2 - 8k_t^2}$. The minimum LR given at $\bar{\kappa}_0$ is given as:

$$LR_{min} = 2\pi^2 B_0 R_0 = \frac{\pi\bar{\kappa}_0\gamma_0}{4Q_M k_t^2} \tag{9}$$

where $B_0 = fC_p/G$ and $R_0 = RG$, each of which can be expressed as functions of only material properties. This minimization is further detailed in [4].

B. Minimum Loss Ratio Scaling

The addition of L_m to the BVD circuit model scales the maximum-efficiency operating point (and the entirety of the impedance plot with it) monotonically as:

$$\frac{\bar{\kappa}_{0,m}}{\bar{\kappa}_{0,bare}} = \mathbb{R}_{\bar{\kappa}_0} = \frac{1}{\sqrt{1+2\Lambda}}, \tag{10}$$

as shown in Fig. 8, where $\mathbb{R}_{\bar{\kappa}_0}$ is a scaling ratio between the augmented and bare PR for κ_0, and

$$\Lambda = \beta \frac{\rho_m}{\rho} \tag{11}$$

We define Λ as the "mass factor", which represents the ratio of the added mass to the PR layer mass. Λ is generally an independent variable.

It has been assumed that the added mass layer acts as a rigid body and does not deform. Therefore, we assume all mechanical loss occurs in the piezoelectric material. This means that the value of R is the same in Figs. 3 and 6. Because the minimum loss ratio can be written as a function of R_0 and B_0 (the forms of which remain unaffected by the addition of the mass layer(s)), the form of the minimum LR is also unchanged. However, this form contains $\bar{\kappa}_0$ in its numerator, so the minimum LR decreases with the following dependence on Λ:

$$\frac{LR_{min,m}}{LR_{min,bare}} = \mathbb{R}_{\text{LR}} = \mathbb{R}_{\bar{\kappa}_0} = \frac{1}{\sqrt{1+2\Lambda}} \tag{12}$$

Thus, loss ratio decreases monotonically with the size of the added mass (and by extension increases efficiency) as shown in Fig. 8.

IV. Effects of Augmentation on Power Density

The addition of mass layers on the dynamic ends of a PR (where the magnitude of displacement is greatest) increases power density through inertial energy storage. This increase in power density results from the fact that the the entirety of the extra mass displaces at the PR's maximum amplitude and also from the increased density of the mass itself. In this section, we model the scale of this effect on power density.

A. Geometry-Normalized Maximum Amplitude of Resonance

The amplitude of resonance model detailed in [4], [6] describes a PR's resonant behavior for a given converter control sequence and operating point. Through this model, it is shown in [4] that the power density capability of a PR depends quadratically on the geometry-normalized form of its maximum current amplitude, I_{Lmaxo}. I_{Lmaxo} can be related to a PR's state variables through:

$$I_{Lmax0} = \Delta_{max} e_{33} v_a \kappa \sin(\kappa_0) \tag{13}$$

where Δ_{max} may be based on material limits (failure stress, coercive electric field, etc.) or practical limits (heat dissipation, failure of adhesive layers, etc.). Thus, maximum power density considering these limits can be calculated through (13).

With mass augmentation, (13) remains the same, but the forms of the state variables T and E are affected by the added mass layer. The relationship between Δ_{max} and T_{max} or E_{max} has dependence on Λ and coupling factor k_t, so the mass-augmented expressions for $I^T_{L0,max}$ and $I^E_{L0,max}$ also depend on Λ and k_t. The scaling of $I^{T,E}_{Lmax0}$ with mass augmentation is therefore a function of only these parameters and can be defined as:

$$\mathbb{R}^{\text{T,E}}_{\text{I}_{\text{Lmax0}}} = \frac{I^{T,E}_{Lmax0,m}}{I^{T,E}_{Lmax0,bare}} \tag{14}$$

where a superscript indicates which material state limits I_{Lmax0}, and the forms of these limits are displayed in Table IV. Figs. 9(a) and 9(b) plot $\mathbb{R}^{\text{T}}_{\text{I}_{\text{Lmax0}}}$ and $\mathbb{R}^{\text{E}}_{\text{I}_{\text{Lmax0}}}$ as functions of Λ for various k_t. For thickness extensional mode, $\mathbb{R}^{\text{T}}_{\text{I}_{\text{Lmax0}}}$ and $\mathbb{R}^{\text{E}}_{\text{I}_{\text{Lmax0}}}$ both monotonically decrease with respect to Λ.

Rather than material limits, I_{Lmax0} may also be limited by a maximum loss density H_{max} (in $\frac{W}{m^2}$) for a given thermal design. In [4], it is shown that:

$$I^H_{Lmax0} = \sqrt{\frac{2}{R_0} H_{Max}} \tag{15}$$

As justified in Section III, the addition of mass is assumed to have no effect on R, and by extension R_0. Therefore, I^H_{Lmax0} is independent of Λ and $\mathbb{R}^{\text{H}}_{\text{I}_{\text{Lmax0}}} = 1$. Table IV contains the functional forms of $I^T_{Lmax0,m}$, $I^E_{Lmax0,m}$, and $I^H_{Lmax0,m}$ for both bare and augmented PRs.

B. Volumetric Energy Handling Density

The volumetric energy handling density is defined as the energy delivered to the load during one cycle, $\frac{P_{out}}{f}$, divided by the volume of the PR, vol:

$$VED = \frac{P_{out}}{f * vol} \tag{16}$$

In the bare case $vol_{bare} = 8abl$ and in the augmented case $vol_m = 8abl(1+\beta)$.

In [4], it is shown that VED can be maximized over l using the amplitude of resonance model, resulting in:

$$VED_{max} = \frac{I^2_{L0,max}}{4\pi\bar{\kappa}_0 v_a B_0} = \frac{I^2_{L0,max}}{\bar{\kappa}_0^2 \epsilon^S_{33} v_a^2} \tag{17}$$

The LR minimization over G in (9) and the VED maximization over l in (17) are orthogonal, so both of these geometry conditions can be satisfied *simultaneously* in a PR design.

As shown in [4], the volumetric power densities of most PRs operating in the thickness extensional mode are limited by loss density. Thus, we investigate the effect of mass augmentation for the loss-density-limited case. Because the VED maximization is independent of the PR's state variables, the form of (17) remains unchanged with mass augmentation except for the additional volume of the added mass, requiring volume to be scaled by $(1+\beta)$. I^H_{Lmax0} is independent of Λ, but $\bar{\kappa}_0^2$ in the denominator depends on Λ according to (10). Thus, VED scales as follows for the H-limited case:

$$\frac{VED^H_{max,m}}{VED^H_{max,bare}} = \mathbb{R}^{\text{H}}_{\text{VED}} = \frac{1+2\Lambda}{1+\beta} = \frac{1+2\Lambda}{1+\frac{\rho}{\rho_{\text{m}}}\Lambda} \tag{18}$$

As shown in Fig. 10, the loss-limited volumetric energy handling density increases monotonically towards a set limit:

$$\lim_{\Lambda \to +\infty} \mathbb{R}^{\text{H}}_{\text{VED}} = 2\frac{\rho_{\text{m}}}{\rho} \tag{19}$$

An important insight gained through (19) is that the mass material should be as dense as possible (consistent with not introducing undue loss), as this increases the slope of the central part of the curve of Fig. 10 and raises the upper limit of improvement.

For the stress and E-field limited cases, $I_{L0,max}$ is no longer independent of Λ. In these cases:

$$\mathbb{R}^{\text{T,E}}_{\text{VED}} = (\mathbb{R}^{\text{T,E}}_{\text{I}_{\text{Lmax0}}})^2 \frac{1+2\Lambda}{1+\frac{\rho}{\rho_{\text{m}}}\Lambda} \tag{20}$$

TABLE IV
GEOMETRY-NORMALIZED MAXIMUM AMPLITUDES OF RESONANCE

	I^T_{Lmax0}	$I^E_{L0,max}$	I^H_{Lmax0}
Non-Augmented	$\frac{e_{33}v_a}{c^D_{33}}\cot(\frac{\bar{\kappa}_0}{2})T_{max}$	$k_t^2\epsilon^S_{33}\frac{\sin(\bar{\kappa}_0)}{\cos(\bar{\kappa}_0)-k_t^2}v_aE_{max}$	$\sqrt{4Q_M\frac{\epsilon^S_{33}k_t^2v_a}{\gamma_0}}H_{max}$
Mass-Augmented	$\frac{e_{33}v_a}{c^D_{33}}\frac{\sin(\bar{\kappa}_0)}{1-\cos\bar{\kappa}_0+\Lambda\bar{\kappa}_0\sin(\bar{\kappa}_0)}T_{max}$	$k_t^2\epsilon^S_{33}\frac{\sin(\bar{\kappa}_0)}{\cos(\bar{\kappa}_0)-k_t^2-\Lambda\bar{\kappa}_0\sin(\bar{\kappa}_0)}v_aE_{max}$	$\sqrt{4Q_M\frac{\epsilon^S_{33}k_t^2v_a}{\gamma_0}}H_{max}$

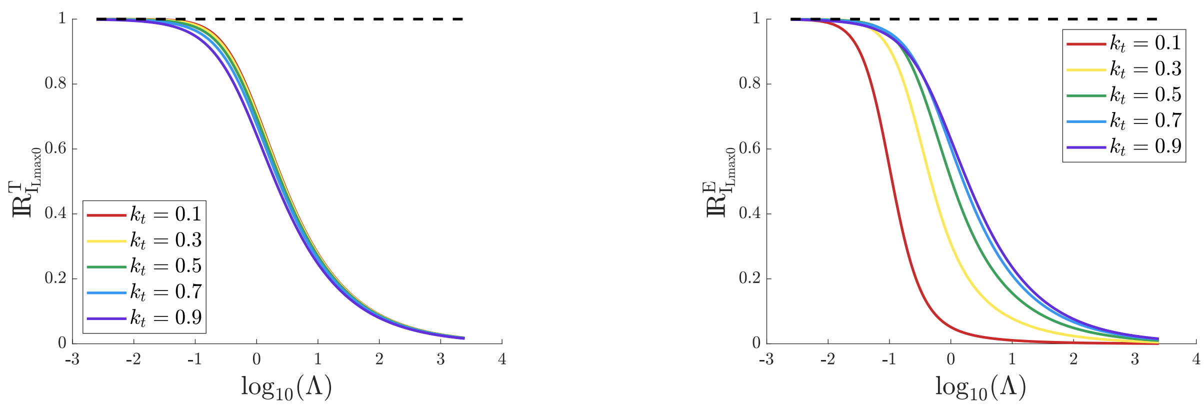

(a) (b)

Fig. 9. (a) Stress-limited geometry-normalized I_{Lmaxo} scaling as a function of Λ for various k_t. (b) E-field-limited geometry-normalized I_{Lmaxo} scaling as a function of Λ for various k_t.

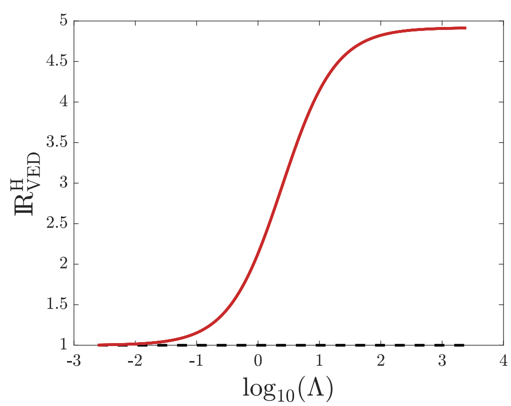

Fig. 10. H-limited volumetric energy handling density scaling as a function of Λ, where $2\frac{\rho_m}{\rho} = 4.9172$

Although $\mathrm{IR}^{\mathrm{T,E}}_{\mathrm{VED}}$ (as shown in Fig. 11a(a)) does not monotonically increase, there is some benefit in an initial region where the magnitude of decreasing $\bar{\kappa}_0$ is greater than the additional loss from $\mathrm{IR}^{\mathrm{T,E}}_{\mathrm{I_{Lmax0}}}$. This means that there is an ideal Λ for maximizing I_{Lmax0} when limited by stress or E-field.

C. Areal Power Density

The areal power density is defined as P_{out} divided by the electrode area:

$$APD = \frac{P_{out}}{4ab} \tag{21}$$

It is shown in [4] that maximum APD with respect to l has the following form, according the amplitude of resonance model:

$$APD_{max} = \frac{I^2_{L0,max}}{4\pi^2 B_0} = \frac{I^2_{L0,max}}{\pi\kappa_0\epsilon^S_{33}v_a} \tag{22}$$

The electrode area is independent of the PR's thickness dimension, l. Therefore, the form of APD_{max} remains unchanged with mass augmentation. In the loss-density-limited case, scaling of APD_{max} is completely dependent on the $\bar{\kappa}_0$ in its denominator. Thus:

$$\frac{APD^H_{max,m}}{APD^H_{max,bare}} = \mathrm{IR}^{\mathrm{H}}_{\mathrm{APD}} = \sqrt{1+2\Lambda} \tag{23}$$

APD_{max} monotonically increases with respect to Λ.

For the stress-limited and E-field-limited cases, I_{Lmax0} is not independent of Λ. These limits scale with:

$$\mathrm{IR}^{\mathrm{T,E}}_{\mathrm{APD}} = (\mathrm{IR}^{\mathrm{T,E}}_{\mathrm{I_{Lmax0}}})^2\sqrt{1+2\Lambda} \tag{24}$$

This trend is similar to that of $VED^{T,E}_{max}$ in Fig. 11; $APD^{T,E}_{max}$ does not monotonically increase, and there is an ideal Λ for which $APD^{T,E}_{max}$ is maximized.

V. AUGMENTED PIEZOELECTRIC RESONATOR DESIGN

It has now been shown that mass-augmented PRs can operate with higher efficiency and power density capabilities than their bare counterparts. This implies that it is possible to design a composite energy storage component that is functionally-equivalent to a bare PR (serving the same voltage, current, and power) at a smaller size.

The design process of a mass-augmented PR begins with the selection of a mass factor, Λ. As determined in [4],

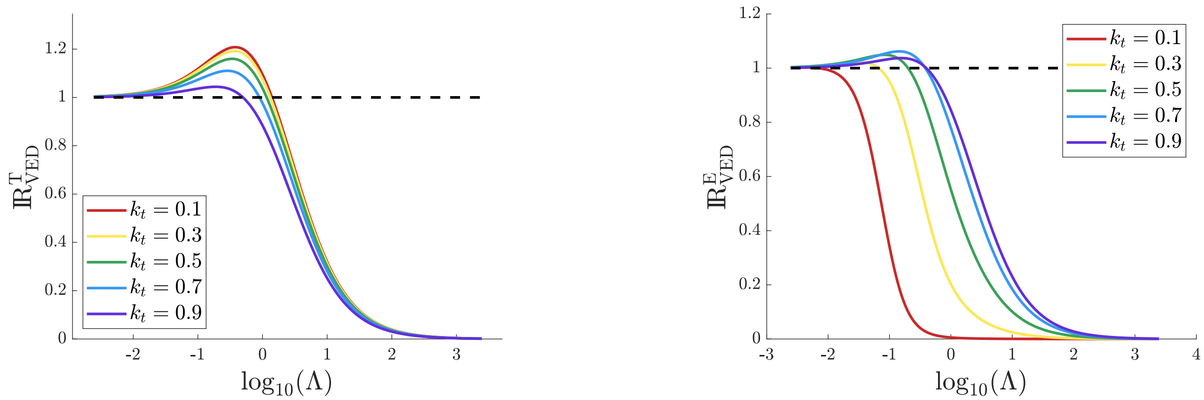

(a) (b)

Fig. 11. (a) Stress-limited volumetric energy handling density scaling as a function of Λ for various k_t. (b) E-Field-limited volumetric energy handling density scaling as a function of Λ for various k_t.

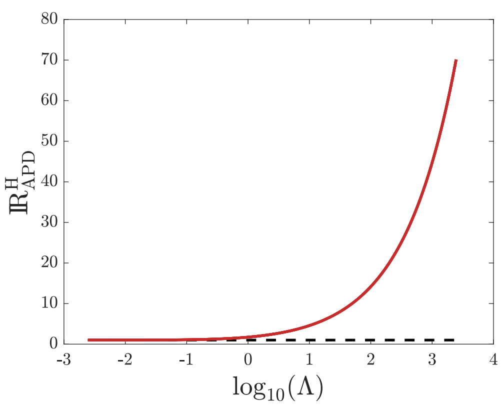

Fig. 12. H-limited areal power density scaling as a function of Λ.

I^H_{Lmax0} is the lowest of the amplitude of resonance limits for most bare PRs. However, as Λ increases, I^T_{Lmax0} and I^E_{Lmax0} decrease until they eventually surpass I^H_{Lmax0} and become the dominant system limits as illustrated in Fig. 13. Λ should be selected to be as high as possible before such limits become relevant, which can be considered the intersection of I^H_{Lmax0} and I^T_{Lmax0} or I^E_{Lmax0}. This point is highlighted for the example in Fig 13.

Once Λ has been selected, the validity of the rigid body assumption must also be verified through the following rigid body condition:

$$\Phi = \frac{\rho}{\rho_m}\frac{c^D_{33}}{c_{33,m}}\frac{\Lambda^2}{1+2\Lambda}\bar{\kappa}^2_{0,bare} << 1 \tag{25}$$

If $\Phi \gtrsim 0.1$, loss due to wave propagation through the added mass may be considered non-negligible. A further explanation and justification for this rigid body condition is included in Appendix A.

l and G should then be selected to satisfy the conditions for maximum power density and minimum loss ratio, respectively, for a nominal operating point. For this step, we recommend use of an improved model for $\bar{\kappa}_0$ as further described in Appendix A. These geometry conditions correspond directly to the extrema of efficiency and power density, a strategy further detailed in [4]:

$$\hat{l} = V_{in}\frac{\kappa_0 v_a \epsilon^S_{33}}{2I^{LD}_{L0,max}} \tag{26}$$

$$\hat{G} = \frac{P_{out}}{V^2_{in}}\frac{4\pi}{\kappa_0 v_a \epsilon^S_{33}} \tag{27}$$

where l and G correspond to the PR's thickness and electrode area, respectively (with $G = \frac{4ab}{l^2}$).

In $\hat{l}$ and $\hat{G}$, all but $\bar{\kappa}_0$ is independent of Λ. Because $\bar{\kappa}_0$ decreases with Λ, it is evident that a larger mass factor results in a thinner, more planar component (i.e., $\frac{4ab}{l^2}$ increases).

An important note is that there is a minimum total thickness $(l + \beta l)$ for the augmented component that occurs at approximately $\beta = 1 - \frac{\rho}{\rho_m}$. If the added material is the same density or less dense than the original material, the overall thickness of the device increases. On the other hand, the electrode area, $4ab$, decreases monotonically. Therefore, component thickness may be minimized through selection of β if the associated Λ remains under the aforementioned limits.

VI. Validation via Simulation

Using the design procedure described in [4], we design a bare PZT-8 PR to operate at $V_{in} = 100$ and $P_{out} = 1kW$ in the topology of Fig. 1. We then design a tungsten-mass-augmented PZT-8 PR for the same nominal V_{in} and P_{out} using the methodology established in Section V. We select tungsten as the non-piezoelectric mass layer material for its high stiffness and density compared to PZT-8. The material properties used for PZT-8 and tungsten can be found in Table V (based on those in COMSOL's material library).

As in Section V, the design process of the mass-augmented PR begins with selecting a value for Λ. As shown in Fig. 13, we choose Λ based on the point at which I_{Lmaxo} becomes stress-limited (i.e., at the intersection of I^L_{Lmaxo} and I^T_{Lmaxo} with respect to Λ). For the nominal operating point, this

TABLE V
MATERIAL PROPERTIES OF PZT-8 AND TUNGSTEN

PZT-8			Tungsten		
ρ	7600	$\frac{kg}{m^3}$	ρ_m	17800	$\frac{kg}{m^3}$
$\frac{\epsilon_{33}^S}{\epsilon_0}$	4.972	$\frac{nF}{m}$	$c_{33,m}$	460	GPa
c_{33}^D	131.7	GPa	σ_m	0.28	
e_{33}	13.91	$\frac{C}{m^2}$			
Q_M	1000				
T_{max}	30	MPa			
E_{max}	7	$\frac{kV}{mm}$			

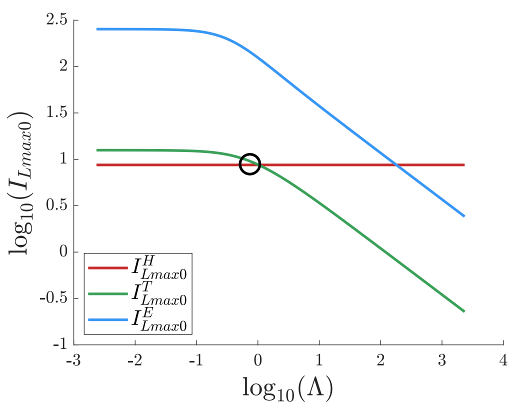

Fig. 13. I_{Lmax0} based on the different limits on the PR vs Λ. The lowest I_{Lmax0} for a given Λ serves as the limit to the system at that point. We choose a value of Λ at the boundary between I_{Lmaxo}'s stress and loss limit ($\Lambda = 0.9$). This example uses PZT-8 and assumes $H = 1\frac{W}{cm^2}$.

TABLE VI
BARE AND AUGMENTED PR DESIGN PARAMETERS

	Bare	Augmented	$\frac{\text{Augmented}}{\text{Bare}}$
PZT-8 Thickness	$202\mu m$	$133\mu m$	0.562
Total Thickness	$202\mu m$	$157\mu m$	0.777
Electrode Area	$14.5cm^2$	$8.18cm^2$	0.562
Width (Square)	$1.91cm$	$1.43cm$	0.749
Volume	$0.587cm^3$	$0.256cm^3$	0.436
Mass	$4.46mg$	$2.68mg$	0.599
Operating Frequency	$5.57MHz$	$5.57MHz$	1
Model LR	0.0146	0.0082	0.562

$V_{in} = 100V$, $P_{out} = 1kW$, $\frac{\rho_m}{\rho} = 2.34$, $\beta = 0.384$, $\Lambda = 0.9$

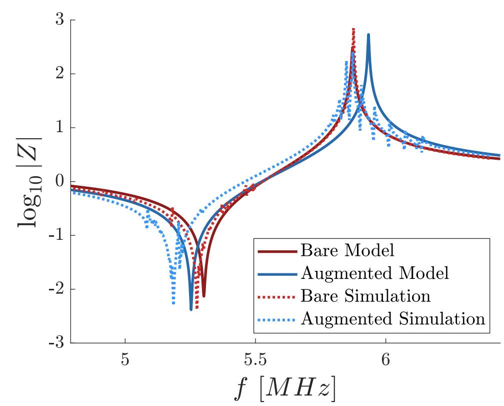

Fig. 14. Thickness extensional impedance amplitude of a bare PR design, equivalent mass-augmented design, and their respective simulations.

requires $\Lambda = 0.9$ and a corresponding $\beta = 0.384$. We also find $\Phi = 0.0899 < 0.1$, which satisfies the rigid body condition. We then use the chart in Fig. 15 to select $\alpha = 1.17$, and follow the design methodology in Section V to choose the length scales of the mass-augmented PR.

We simulate these two designs in the frequency domain using COMSOL, and their resulting impedance characteristics are shown in Fig. 14 along with their modeled impedances. The proposed model is shown to fit the simulated impedance data well, and the two designs have near-equivalent resonant frequencies and inductive regions. Table VI compares these two designs and shows that the resulting mass-augmented PR has only 56% the footprint area and 44% the volume of the bare PR, amounting to a 78% increase in areal power density and a 130% increase in volumetric power density. Additionally, the mass-augmented PR has the same ideal operating frequency with 56% less power loss. This validates mass augmentation as a promising means to drastically reduce PR size while retaining functionality and improving efficiency.

VII. CONCLUSION

Augmenting PRs with non-piezoelectric mass layers can result in smaller, lighter, and more efficient passive components for power conversion. For PRs constrained by loss, mass-augmentation increases efficiency, areal power density, and volumetric energy handling density monotonically with the mass layer's relative size. These advantages (which have been verified through simulation) build upon those already established for bare PRs, suggesting PR augmentation to be a promising path forward for miniaturized power conversion.

APPENDIX A
IMPROVED TANGENT APPROXIMATION

In order to relate the modified BVD circuit model to the constitutive model of the PZT, the tangent terms in the augmented PR's impedance

$$Z_m = \frac{1}{\epsilon_{33}(j\omega)}\frac{l}{2ab}\left[\frac{1-(k_t^2+\Lambda\kappa_0^2)\frac{\tan\kappa_0}{\kappa_0}}{1-\Lambda\kappa_0^2\frac{\tan\kappa_0}{\kappa_0}}\right] \quad (28)$$

are approximated using the first term of the partial fraction expansion for $\tan(x)$:

$$\tan(x) \approx \frac{8x}{\pi^2-4x^2} \quad (29)$$

However, due to the $\Lambda\kappa_0^2$ terms in the form of Z_m, errors approximation around $\tan x$ can cause large deviations in the location of the resonant and anti-resonant frequencies of the approximated and non-approximated impedances. For this reason, it is beneficial to scale the tangent approximation by an error-reduction factor, α. In the main body of this paper we utilize the non-improved model because it gives a better intuitive understanding of the affect of added mass on a PR.

Applying α results in the following expression for the maximum-efficiency geometry-normalized wave number:

$$\bar{\kappa}_0 = \frac{\pi\sqrt{\pi^2-8\alpha k_t^2}}{\pi+\sqrt{\pi^2-8\alpha k_t^2}}\sqrt{\frac{1}{1+2\alpha\Lambda}} \quad (30)$$

The value of α can be numerically obtained by setting the form of the non-approximated resonant and anti-resonant

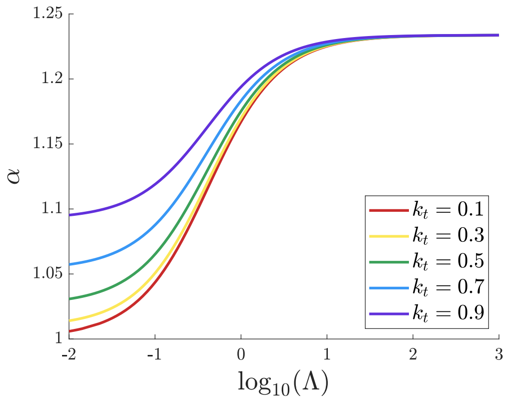

Fig. 15. A map for choosing α. For large values of k_t, this corrects error in even the bare PR case. As Λ increases, α approaches a constant value $\alpha = 1.234$.

frequencies to their newly-approximated counterparts. This results in two values for α which can be averaged to minimize error on both ends of the inductive region. Fig. 15 contains a chart of α for different values of Λ and k_t.

Appendix B
Rigid Body Condition

In this work, we assume the mass can be treated as a rigid body. In this section, we quantify the validity of this assumption. For this we turn to dimensional analysis (although the same quantity of relevance can also be found through lumped-element analysis or other similar methods).

The length of the mass layer is βl, and we take $x_3 = 0$ to be at the center of the bare PR. For this derivation, the system of interest is the layer of mass attached to the PR from $x_3 = l$ to $x_3 = l + \beta l$. This layer of material is purely elastic (not piezoelectric), so we assume a linear elastic wave equation in the layer. This equation can then be non-dimensionalized through use of a time scale $\tau = \frac{1}{\omega} = \frac{l}{v_a \kappa_0}$ and length scale $\bar{L} = \beta l$. The non-dimensionalized variables become:

$$u^* = \frac{u_3(x_3, t)}{u_3(x_3 = l, t = 0)} \qquad x^* = \frac{x_3}{\beta l} \qquad t^* = \frac{v_a \kappa_0}{l} t \tag{31}$$

This results in the non-dimensionalized wave equation:

$$\frac{\partial^2 u^*}{\partial x^{*2}} - \Phi \frac{\partial^2 u^*}{\partial t^{*2}} = 0 \tag{32}$$

We define the dimensionless parameter:

$$\Phi = \frac{v_a^2}{v_{a,m}^2} \beta^2 \kappa_0^2 \tag{33}$$

as the parameter of interest in the validity of the rigid body assumption. We have designed the time and length non-dimensionalization factors, τ and $\bar{L}$ so that $\frac{\partial^2 u^*}{\partial x^{*2}}$ and $\frac{\partial^2 u^*}{\partial t^{*2}}$ must always be of order $O(1)$. If we take a closer look at (17), this implies that if $\Phi << 1$, $\frac{\partial^2 u_3}{\partial x_3^2} \approx 0$, which in turn implies the form:

$$u_3 = A x_3 + B \tag{34}$$

Once we apply the boundary conditions, we recover the equation for a rigid body (constant displacement in space):

$$u_3(x_3, t) = \Delta \sin(\kappa_0) e^{j\omega t} \qquad l < x_3 < l + \beta l \tag{35}$$

Thus, the condition for treating the mass layer as a rigid body is $\Phi << 1$. It is also important to note that for a mass-augmented PR, Φ can be written as:

$$\Phi = \frac{\rho}{\rho_m} \frac{c_{33}^D}{c_{33,m}} \frac{\Lambda^2}{1 + 2\Lambda} \bar{\kappa}_{0,bare}^2 \tag{36}$$

where $\bar{\kappa}_{0,bare}$ is the bare PR dimensionless wave number. From this it is clear that as the relative size of the mass layer is increased, its relative stiffness is decreased, or its relative density decreased, the point mass assumption will begin to break down. This is not to say that additional mass is no longer useful, but that additional effects such as changes to the mass boundary condition and loss due to wave propagation through the mass layer must be considered as part of the modeling and composite component design.

References

[1] D. J. Perreault, J. Hu, J. M. Rivas, Y. Han, O. Leitermann, R. C. Pilawa-Podgurski, A. Sagneri, and C. R. Sullivan, "Opportunities and challenges in very high frequency power conversion," in *Proc. IEEE Applied Power Electronics Conference and Exposition*, Washington, DC, USA, Feb. 2009, pp. 1–14.

[2] C. R. Sullivan, B. A. Reese, A. L. Stein, and P. A. Kyaw, "On size and magnetics: Why small efficient power inductors are rare," in *Proc. IEEE Intl. Symposium on 3D Power Electronics Integration and Manufacturing*, Raleigh, NC, USA, Jun. 2016, pp. 1–23.

[3] P. A. Kyaw, A. L. Stein, and C. R. Sullivan, "Fundamental examination of multiple potential passive component technologies for future power electronics," *IEEE Transactions on Power Electronics*, vol. 33, no. 12, pp. 10,708–10,722, 2018.

[4] J. D. Boles, J. E. Bonavia, P. L. Acosta, Y. K. Ramadass, J. H. Lang, and D. J. Perreault, "Evaluating piezoelectric materials and vibration modes for power conversion," *IEEE Transactions on Power Electronics*, vol. 37, no. 3, 2022.

[5] B. Pollet, G. Despesse, and F. Costa, "A new non-isolated low power inductorless piezoelectric dc-dc converter," *IEEE Transactions on Power Electronics*, vol. 34, no. 11, pp. 11 002–11 013, 2019.

[6] J. D. Boles, J. J. Piel, and D. J. Perreault, "Enumeration and analysis of dc-dc converter implementations based on piezoelectric resonators," *IEEE Transactions on Power Electronics*, vol. 36, no. 1, pp. 129–145, 2021.

[7] W. Braun, E. Stolt, L. Gu, J. J. Segovia-Fernandez, S. Chakraborty, R. Lu, and J. M. R. Davila, "Optimized resonators for piezoelectric power conversion," *IEEE Open Journal of Power Electronics*, 2021.

[8] M. Touhami, G. Despesse, and F. Costa, "A new topology of dc-dc converter based on piezoelectric resonator," in *2020 IEEE 21st Workshop on Control and Modeling for Power Electronics (COMPEL)*. IEEE, 2020, pp. 1–7.

[9] J. D. Boles, E. Ng, J. H. Lang, and D. J. Perreault, "Dc-dc converter implementations based on piezoelectric transformers," *Journal of Emerging and Selected Topics in Power Electronics*, 2022.

[10] K. S. Van Dyke, "The piezo-electric resonator and its equivalent network," *Proceedings of the Institute of Radio Engineers*, vol. 16, no. 6, pp. 742–764, 1928.

[11] J. Erhart, P. Půlpán, and M. Pustka, *Piezoelectric Ceramic Resonators*. Springer, 2017.

[12] S. J. Martin, V. E. Granstaff, and G. C. Frye, "Characterization of a quartz crystal microbalance with simultaneous mass and liquid loading," *Analytical chemistry*, vol. 63, no. 20, pp. 2272–2281, 1991.

[13] A. Fort, E. Panzardi, V. Vignoli, M. Tani, E. Landi, M. Mugnaini, and P. Vaccarella, "An adaptive measurement system for the simultaneous evaluation of frequency shift and series resistance of qcm in liquid," *Sensors*, vol. 21, no. 3, p. 678, 2021.